Functional imaging of dye concentration in tissue phantoms by spectroscopic optical coherence tomography

Trude Støren
Norwegian University of Science and Technology
Department of Physics
N-7491 Trondheim, Norway

Arne Røyset
SINTEF Materials Technology
Department of Applied Physics
N-7465 Trondheim, Norway

Lars O. Svaasand
Norwegian University of Science and Technology
Department of Electronics and Telecommunications
N-7491 Trondheim, Norway

Tore Lindmo
Norwegian University of Science and Technology
Department of Physics
N-7491 Trondheim, Norway
E-mail: Tore.Lindmo@phys.ntnu.no

Abstract. We present functional imaging of the concentration of a photodynamic therapy (PDT)-related dye in scattering tissue phantoms based on spatially resolved measurements of optical properties through spectroscopic optical coherence tomography (OCT). Expressions for the OCT signal are developed, enabling estimation of depth-resolved sample optical properties. Based on these expressions, we discuss speckle statistics and speckle correlations of the OCT signal. Speckle noise reduction is performed by spatial filtering and is used to improve accuracy in the estimated optical properties at the expense of spatial resolution. An analytic expression for the precision in the estimated optical properties is derived. This expression shows that axial filtering, and thereby a reduction of axial resolution, gives a larger improvement in precision compared to the same filtering and reduction in the transversal resolution. It also shows that imaging with a shorter coherence length, or a larger numerical aperture, improves precision when the filter length determines the spatial resolution. Good agreement is obtained between experimentally determined and theoretically predicted variance in the estimated attenuation coefficients and dye concentration. Finally, we present guidelines for spectroscopic OCT systems for concentration imaging and discuss application of the method to more realistic phantoms and tissue. [DOI: 10.1117/1.1898242]

Keywords: optical coherence tomography; speckle; concentration monitoring; photodynamic therapy; optical properties; functional imaging.

Paper 04030 received Mar. 5, 2004; revised manuscript received Aug. 12, 2004; accepted for publication Aug. 17, 2004; published online Apr. 29, 2005.

1 Introduction

Optical coherence tomography (OCT) has become a well-established technique for obtaining high-resolution structural images of biological and other semitransparent tissues. The introduction of extremely broadband, highly coherent sources[1,2] and the development of full-field OCT instruments using affordable white light sources[3] enables the imaging resolution to approach that of histology. This increases the value of OCT as a diagnostic tool and has brought OCT closer to the goal of performing noninvasive optical biopsies.

OCT has recently been expanded to different functional imaging modalities such as Doppler OCT, where velocity in a fluid flow can be determined with high spatial resolution,[4] polarization sensitive OCT for, e.g., imaging of sample birefringence,[5] molecular imaging,[6,7] and spectroscopic[8–11] OCT.

Several authors have addressed the challenge of extracting quantitative information on optical properties from scattering samples using low-coherence reflectometry (LCR) and OCT. In 1993 Schmitt et al.[12] studied the relationship between optical properties of a homogeneous scattering sample and the signal measured by LCR. Publications by Pan et al.,[13] Schmitt and Knüttel,[14] and Thurber et al.[15] give comprehensive models of the LCR signal detected from a scattering sample. In a recent publication, Kholodnykh et al.[16] studied how speckle averaging improves the precision of the estimated attenuation coefficient of tissue.

Using one wavelength channel it is possible to obtain information about only the attenuation in the sample, i.e., the sum of absorption and scattering. Spectroscopic OCT, using two or more wavelengths, enables separation of scattering from absorption, making it possible to monitor the concentration of an absorbing analyte in a scattering sample.[9,17–19] This requires knowledge of the difference in absorption of the sample at the probing wavelengths. An application of concentration imaging could be monitoring the diffusion of a topically applied sensitizer prior to light exposure in photodynamic therapy[20] (PDT).

It is well known that OCT images, like all other images obtained using coherent light, contain speckle noise. A study of image formation in OCT shows that speckle is both the information carrier and a source of noise degrading image

Address all correspondence to Dr. Tore Lindmo, Norwegian University of Science and Technology, Department of Physics, N-7491 Trondheim, Norway. E-mail: Tore.Lindmo@phys.ntnu.no

1083-3668/2005/$22.00 © 2005 SPIE

quality. Much work has concentrated on suppressing speckle noise in OCT images and thereby increasing image SNR. Excellent reviews of the origin of speckle noise and different approaches to speckle noise reduction are given in articles by Schmitt et al.,[21] Fercher et al.,[22] and Pircher et al.[23] Less work has been done related to the effect and suppression of speckle noise in imaging of optical properties. Care must be taken to ensure that the speckle reduction method does not adversely affect quantitative estimation of the optical properties.[12,16]

In this paper, functional imaging of the concentration of an analyte in scattering tissue phantoms is obtained through spatially resolved measurements of optical properties of the phantom by means of spectroscopic OCT. Spatial averaging is used to improve accuracy in the estimated optical properties at the expense of spatial resolution. We present a quantitative analysis of the limitations on axial and transversal resolution in the images due to speckle noise and discuss the practical consequences of these limitations for the usefulness of such functional imaging.

2 Theory

2.1 *Sample Optical Properties*

Attenuation of light propagating in an absorbing and scattering medium is governed by the total attenuation coefficient

$$\mu_{t\lambda}(\mathbf{r}) = \mu_{a\lambda}(\mathbf{r}) + \mu_{s\lambda}(\mathbf{r}), \tag{1}$$

where $\mu_{a\lambda}(\mathbf{r})$ and $\mu_{s\lambda}(\mathbf{r})$ are the absorption and scattering coefficients of the medium, respectively, generally functions of wavelength and position. It was previously shown that μ_t can be extracted from OCT measurements as long as the light contributing to the OCT signal is dominated by single-backscattered photons.[12,16,24]

Consider a scattering sample containing an absorbing dye having concentration C_{dye}, e.g., tissue with an applied photosensitizer. As long as the dye is the only absorbing component in the sample, the relationship between dye concentration and sample absorption coefficient $\mu_{a,\lambda}$ is given by the wavelength-dependent extinction coefficient $\epsilon_{a,\lambda}$ as

$$\epsilon_{a,\lambda} = \frac{\mu_{a,\lambda}}{C_{\mathrm{dye}}}. \tag{2}$$

Assuming that the scattering coefficients at two wavelengths λ_1 and λ_2 are proportional, and that the parameter F is given by

$$F = \frac{\mu_{s,\lambda_1}}{\mu_{s,\lambda_2}}, \tag{3}$$

the dye concentration can be expressed in terms of the attenuation coefficients at the two wavelengths as

$$C_{\mathrm{dye}}(\mathbf{r}) = \frac{\mu_{t,\lambda_1}(\mathbf{r}) - \mu_{t,\lambda_2}(\mathbf{r})F}{\epsilon_{a,\lambda_1} - \epsilon_{a,\lambda_2}F}. \tag{4}$$

The simple form of Eq. (4) is due to the assumption that F and μ_s are independent of the dye concentration, i.e., the presence of the dye does not change the scattering properties of the sample. The equation is also limited to the case where the dye under study is the only absorbing component in the sample. When measuring the concentration of a dye in live tissue, these assumptions will no longer necessarily be valid, thus complicating the analysis. For live tissue, other chromophores (e.g., hemoglobin and melanin) may contribute to the absorption, and the wavelength dependence of the scattering will probably not be as simple as assumed in Eq. (3). In spite of these challenges, we expect that as long as a known relationship exists between the scattering and the dye concentration, it will be possible to find an expression for the dye concentration based on measurements of the attenuation coefficient at two wavelengths. Note that in the case of $\epsilon_{a,\lambda_1} = F\epsilon_{a,\lambda_2}$, i.e., the ratio between the absorption coefficients at the two probing wavelengths equals the ratio between the scattering coefficients, it is not possible to separate scattering from absorption and thus determine C_{dye}.

2.2 *Model of the OCT Signal Received from a Scattering and Absorbing Sample*

Considering a scattering and absorbing sample in a low-coherent interferometer, we now develop expressions for the OCT signal enabling estimation of the depth-resolved attenuation coefficient of the sample. Based on these expressions we discuss speckle statistics and speckle correlations of the OCT signal.

We assume that the interferometer is illuminated by a low-coherent source having a normalized spectral distribution $S(k)$, where $k = 2\pi/\lambda$ is the wave number of the radiation at vacuum wavelength λ. For a source of total intensity I, the intensity at wave number k is $I(k) = IS(k) = |E(k)|^2$, where $E(k)$ is the field. The intensities incident on the sample and reference arms are denoted $I_{0s} = |E_{0s}|^2$ and $I_{0r} = |E_{0r}|^2$, respectively, and the field returning from the reference arm, at wave number k, is

$$E_r(z_r, k) = E_{0r}(k)\exp(i2kz_r), \tag{5}$$

when z_r is the reference arm optical path length. For a reference arm having a reflecting mirror in air, the reference arm optical path length is directly given by the position of the mirror along the optical axis.

The light incident onto the sample is focused at a controlled depth, ensuring that the optical path length in the sample arm, to the focus position, equals the optical path length of the reference arm. The transversal position in the sample (position in the xy plane) is denoted $\mathbf{r}_t$, and the total field, at wave number k, backscattered from the sample can be expressed as

$$E_s(\mathbf{r}_t, z_r, k) = E_{0s}(k)\int_{-\infty}^{\infty} \mathrm{d}z_s \int_{S_{xy}} \mathrm{d}\mathbf{r}_t' J(\mathbf{r}_t - \mathbf{r}_t', z_r - z_s) \times O(\mathbf{r}_t', z_s)\exp(i2kz_s), \tag{6}$$

where z_s is the optical path length in the sample arm corresponding to geometrical sample depth z, $\mathrm{d}\mathbf{r}_t'$ represents the differential surface element for integration over the whole xy plane (S_{xy}), and $J(\mathbf{r}_t, z_s)$ is a focus function describing the phase and amplitude of light backscattered from position $(\mathbf{r}_t, z_s)$ compared to backscattering from position (0,0). The focus function depends on the beam amplitude and phase pro-

file and the focusing optics, and is generally a function of the source center wavelength. The object function $O(\mathbf{r}_t, z_s)$, describes the backscattering and attenuation properties within the sample. The origin of scattering is fluctuations in the sample refractive index. In this paper, we do not model the refractive index fluctuations, but use a simplified scattering model where scattering is represented by discrete point scatterers distributed randomly throughout the sample. Thus, O is a random function of the sample coordinates. The sample has an average refractive index affecting the phase of the radiation propagating through the sample and thus determining the relation between the optical and geometrical sample depth.

The field from the sample arm interferes with the field from the reference arm and the intensity of the combined fields at wave number k is given by $I_{\mathrm{det}}(k)=|E_s(k)+E_r(k)|^2$. The total detected intensity is found by integrating $I_{\mathrm{det}}(k)$ over all k and will be a function of reference arm optical path length z_r and transversal probing-light position $\mathbf{r}_t$:

$$I_{\mathrm{det}}(\mathbf{r}_t, z_r) = I_r + I_s(\mathbf{r}_t, z_r) + 2\,\mathrm{Re}\left\{ E_{0r}E_{0s}^{*}\int_{-\infty}^{\infty} \mathrm{d}z_s \int_{S_{xy}} \mathrm{d}\mathbf{r}_t' O(\mathbf{r}_t', z_s) \times J(\mathbf{r}_t - \mathbf{r}_t', z_r - z_s)\,\gamma[2(z_r - z_s)] \right\}. \quad (7)$$

In Eq. (7) we have used the definition of the normalized, complex coherence function of the source given by $\gamma(z) = \int_0^{\infty} \mathrm{d}k S(k) \exp(-ikz)$. The last term in Eq. (7) is the interference part of the detector intensity, and is denoted I_{int}. We see that I_{int} is two times the real part of a convolution in both $\mathbf{r}_t$ and z_r, between the object function and the product of the focus function and the coherence function. Letting $\otimes$ represent the convolution operation, we write

$$I_{\mathrm{int}}(\mathbf{r}_t, z_r) = 2(I_{0r}I_{0s})^{1/2}\,\mathrm{Re}\{O(\mathbf{r}_t, z_r) \otimes [J(\mathbf{r}_t, z_r)\,\gamma(2z_r)]\} = 2(I_{0r}I_{0s})^{1/2}\,\mathrm{Re}[I_c(\mathbf{r}_t, z_r)]. \quad (8)$$

Equations (7) and (8) show that the complex interferogram $I_c(\mathbf{r}_t, z_r)$, at transversal position $\mathbf{r}_t$ and reference mirror position z_r, is the sum of complex coherence functions centered at the scattering positions in the sample. The amplitudes and phases of the coherence functions are modified by the focus function centered at optical depth z_r and transversal position $\mathbf{r}_t$ in the sample. The interferogram will thus have contributions from a probing volume (voxel) in the sample limited transversally by the focal width l_t. Axially, the voxel will be limited by the shortest of the depth of focus d_f and the coherence length l_c of the source. For a Gaussian beam, the focal width and depth of focus are related to the wavelength and the $1/e^2$ beam divergence angle in the sample θ_0 through the relations $l_t = (2\lambda)/(\pi\theta_0)$ and $d_f = (2\lambda)/(\pi\theta_0^2)$. One common definition of the coherence length is the full width at half maximum (FWHM) of the coherence function given by $l_{c,v} = (2\ln 2/\pi)\lambda_0^2/\Delta\lambda$, where λ_0 and $\Delta\lambda$ are the center wavelength and the FWHM of the source spectrum in vacuum, respectively. In a sample of group refractive index n_g, the coherence length is $l_c = l_{c,v}/n_g$. For sources and numerical apertures commonly used in OCT, the coherence length will be the limiting factor and determine the resolution in the axial direction. The effect of dispersion which may degrade resolution for broadband sources,[25,26] is not included in this analysis.

If the source spectrum is symmetrical about its center frequency, the coherence function in Eq. (8) is a complex function whose amplitude is given by the form of the source spectrum, and phase is given by the source center wavelength. For a scattering sample, the interferogram will be a sum of contributions with randomly distributed phases. Comparing this to established speckle theory we see that the interferogram is a speckle signal with Gaussian statistics, analogous to the field in coherent speckle formation.[27] The axial and transversal correlation lengths in the speckle field (the speckle size) will be given by the axial and transversal resolution l_c and l_t, since these parameters determine the size of the sample probing volume. Moving the probing volume a distance l_c axially or l_t transversally between two measurements will result in measurements containing statistically independent speckle since they represent reflections from essentially independent sets of scatterers.

Recording the interferogram as a function of the optical path length of the reference arm represents imaging as a function of the optical depth of the sample. In the case of a known and relatively simple refractive index distribution, the geometrical depth can be calculated from the optical depth; e.g., in the case of a sample with a constant, average group refractive index n_g, the geometrical sample depth is $z = z_s/n_g$, where z_s is optical sample depth.

In a scattering and absorbing sample, a first-order object function can be expressed as a function of geometrical positions in the sample:

$$O(\mathbf{r}_t, z) = r_\lambda(\mathbf{r}_t, z) \exp\left[-2\int_0^z \frac{1}{2}\mu_{t,\lambda}(\mathbf{r}_t, z')\,\mathrm{d}z' \right], \quad (9)$$

where $r_\lambda(\mathbf{r}_t, z)$ is the complex random field reflectivity of the sample, while the exponential factor describes the two-way attenuation in the sample according to the Beer-Lambert law. The factor 2 is due to the field propagating to depth z and back to the sample surface, and the field attenuation coefficient is half the intensity attenuation coefficient μ_t. In these and the following expressions, the subscript λ denotes the center wavelength of the probing light.

In OCT, it is common to record the envelope $A_\lambda(\mathbf{r}_t, z)$ of the interferogram. While the interferogram of Eq. (8) has Gaussian statistics, the envelope of the interferogram is a Rayleigh-distributed random function.[22,23,28] From Eq. (8) we see that if the exponential factor in the object function of Eq. (9) is slowly decaying compared to the axial speckle size, the envelope of the interferogram averaged over the speckle correlation length, given by the coherence length in the sample, is the envelope of the object function averaged over the same length. The ensemble average $\langle A_\lambda(\mathbf{r}_t, z)\rangle$ of the envelope is thus

$$\langle A_\lambda(\mathbf{r}_t, z)\rangle = G_\lambda \langle |r_\lambda(\mathbf{r}_t, z)|\rangle \exp\left[-\int_0^z \mu_{t,\lambda}(\mathbf{r}_t, z')\,\mathrm{d}z' \right], \quad (10)$$

where G_λ is proportional to the intensity of the light incident in the interferometer, the envelope of the coherence function, and gain factors in the detection system.

When recording 2-D cross-sectional OCT images we use the average envelope of m transversally displaced A scans as image function P_m. In this paper, we do not record 3-D data and will in the following denote the transversal direction as x for simplicity. The image function is defined as

$$P_{m,\lambda}(x,z)=\frac{1}{m}\sum_{i=1}^{m} A_\lambda(x_i,z), \tag{11}$$

where x is the average of the set $\{x_i\}$. The transversal displacement for each A scan is denoted $\Delta x=|x_i-x_{i-1}|$. While, for an envelope dominated by a speckle signal, P_1 is Rayleigh distributed, $P_{m>1}$ will have a gamma distribution, and in the limit of large m become Gaussian distributed.[23,27] Since the image function is a linear function of the OCT envelope, it is straightforward to find the statistical properties of the image function from the statistical properties of the OCT envelope. For all m, the ensemble average of the image function is equal to the ensemble average of the envelope given in Eq. (10), while its variance is reduced by m for statistically uncorrelated A scans, obtained when Δx is larger than the transversal correlation length l_t. Since P_1 is Rayleigh distributed with mean value $\langle A\rangle$, its variance is given by[23]

$$\sigma_{P_1}^2=\left(\frac{4}{\pi}-1\right)\langle A\rangle^2. \tag{12}$$

2.3 *Estimating Optical Properties and Dye Concentration*

We now develop equations used for estimating the attenuation coefficient and thus the dye concentration of a scattering and absorbing sample based on measurements of the depth-resolved envelope at two probing wavelengths. The variance in the estimated dye concentration is dominated by speckle noise, and we derive equations describing how spatial averaging improves precision in the estimated attenuation coefficients and dye concentration.

Taking the natural logarithm of Eq. (10) and differentiating, we obtain

$$\frac{\mathrm{d}}{\mathrm{d}z}\ln\langle A_\lambda(x,z)\rangle=\frac{\mathrm{d}}{\mathrm{d}z}[\ln\langle|r_\lambda(x,z)|\rangle]-\mu_{t,\lambda}(z) \tag{13}$$

when we assume that G_λ is independent of depth. The scattering coefficient of a sample is related to its field reflectivity through the relation[29]

$$\mu_{s,\lambda}(x,z)\propto\langle|r_\lambda(x,z)|^2\rangle. \tag{14}$$

We see that when $\mu_{s,\lambda}(x,z)$ and thus $\langle|r_\lambda(x,z)|\rangle$ is constant or slowly changing as a function of depth, the first term on the right side of Eq. (13) can be neglected, and we are left with the depth-resolved attenuation coefficient of the sample. Substituting the average envelope with the image function we thus get an estimate for the spatially resolved total attenuation coefficient

$$\hat{\mu}_t(x,z;m)=-\frac{\mathrm{d}}{\mathrm{d}z}[\ln P_{m,\lambda}(x,z)], \tag{15}$$

where the hat over the attenuation coefficient indicates the estimate. We return to the field-reflectivity term in the discussion of experimental results.

Due to the nonlinear relationship between the image function and the estimator for the attenuation coefficient, we used simulations to study the statistical properties of the estimator. For the simulation, we create statistically independent data sets representing the OCT envelope by drawing from a Rayleigh distribution. The simulations show that when the image function $P_{m,\lambda}$ is an average of m statistically independent realizations of the OCT envelope, the mean value of the logarithm of the image function is $\langle\ln P_m\rangle=\ln\langle A\rangle-K_1/m$, while the variance is $\sigma^2_{\ln P_m}=K_2/m$. The constants K_1 and K_2 in these empiric relations were found to be $K_1=0.167$ and $K_2=0.41$. We see that while the mean value of $\ln P_m$ depends on the average OCT envelope, the variance is independent of the average OCT envelope. When the envelope mean value has the form of Eq. (10), the estimator of Eq. (15) is an unbiased estimator for the attenuation coefficient since the last term in the empiric expression for $\langle\ln P_m\rangle$ is constant with respect to sample depth, and thus vanishes in the differentiation.

To obtain an accurate spatially resolved estimate of the sample optical properties, averaging is necessary. Due to the nonlinearity in the estimator introduced by the logarithm, we choose to carry out the averaging prior to taking the logarithim. We thus convolve the image function with filter functions $h_z(z)$ and $h_t(x)$ in the axial and transversal directions, respectively. Transversally this averaging is equivalent to the averaging inherent in the definition of the image function for $m>1$. Depending on the transversal sampling rate of the recorded data and the width of the transversal filter function it might be useful to combine a reduction of the data set using an image function having $m>1$ with transversal averaging through convolution. In the case of a constant or slowly varying field reflectivity, a speckle-averaged estimate of the spatially resolved attenuation coefficient is thus given by

$$\begin{aligned}\hat{\mu}_{t,\lambda}(x,z;L_z,L_t)&=-\frac{\mathrm{d}}{\mathrm{d}z}\ln[P_{m,\lambda}(x,z)\otimes h_t(x)\otimes h_z(z)]\\&=-\frac{\mathrm{d}}{\mathrm{d}z}\ln\left[\int_{-\infty}^{\infty}\mathrm{d}x'\int_{-\infty}^{\infty}\mathrm{d}z'\right.\\&\qquad\left.\times P_{m,\lambda}(x',z')h_t(x-x')h_z(z-z')\right]\\&=-\frac{\mathrm{d}}{\mathrm{d}z}\ln[P_{MN,\lambda}(x,z)],\end{aligned} \tag{16}$$

where $P_{MN,\lambda}$ represents an image function averaged over M and N statistically independent speckle realizations in the transversal and axial directions, respectively. The transversal and axial filter functions have characteristic lengths L_t and L_z, respectively (typically full width at half maximum of the filter functions). Thus, M and N can be approximated by

$$M \approx \frac{L_t}{\max(l_t, \Delta x)}, \qquad N \approx \frac{L_z}{l_c}. \tag{17}$$

Essential to measurements of sample optical properties is the precision by which these properties can be determined.[16] We therefore developed an expression for the variance $\sigma^2_{\hat{\mu}t}$ in the estimated attenuation coefficient of Eq. (16). Using the chain rule for differentiation together with the definition of the differential operator, the estimator can be expressed

$$\hat{\mu}_{t,\lambda}(x,z;L_z,L_t) = -\frac{1}{P_{MN,\lambda}(x,z)} \frac{\mathrm{d}P_{MN,\lambda}(x,z)}{\mathrm{d}z} \approx -\lim_{\Delta z \to 0} \frac{P_{MN,\lambda(x,z+\Delta z)} - P_{MN,\lambda}(x,z)}{\Delta z P_{MN,\lambda}(x,z)}. \tag{18}$$

From this expression, the variance of the estimator can be found:

$$\sigma^2_{\hat{\mu}t} = \langle \hat{\mu}_t^2 \rangle - \langle \hat{\mu}_t \rangle^2 \approx \lim_{\Delta z \to 0} \frac{\langle [P_{MN,\lambda(x,z+\Delta z)} - P_{MN,\lambda}(x,z)]^2 \rangle}{\Delta z^2 \langle P_{MN,\lambda}(x,z) \rangle^2} - \langle \hat{\mu}_t \rangle^2. \tag{19}$$

Expressing the averaged image function as a sum of its mean value and a varying part, $P_{MN,\lambda} = \langle P_{MN,\lambda} \rangle + \Delta P_{MN,\lambda}$, and using the fact that the mean value of the image function equals the mean value of the OCT envelope given in Eq. (10), we obtain the following expression:

$$\sigma^2_{\hat{\mu}t} = 2C^2_{P_{MN,\lambda}} \lim_{\Delta z \to 0} \frac{1 - \rho_{\Delta P_{MN,\lambda}}(\Delta z)}{\Delta z^2}, \tag{20}$$

where $C_{P_{MN,\lambda}} = C_{A,\lambda}/\sqrt{MN} = [(4/\pi - 1)/MN]^{1/2}$ is the speckle contrast of the averaged image function, and $\rho_{\Delta P_{MN,\lambda}}(\Delta z) = \rho_{P_{MN,\lambda}}(\Delta z)$ is the autocorrelation of the averaged image function in the axial direction. According to signal processing theory,[30] $\rho_{P_{MN,\lambda}}(\Delta z)$ is found by convolving $\rho_{P_{m,\lambda}}(\Delta z)$, the correlation function for $P_{m,\lambda}(x,z)$ in the axial direction, with the autocorrelation of the filter function h_z. It can be shown that as long as the m A scans averaged to obtain the image function are statistically independent, $\rho_{P_{m,\lambda}}(\Delta z) = \rho_A(\Delta z)$, where $\rho_A(\Delta z)$ is the autocorrelation of the OCT envelope given by the autocorrelation of the envelope impulse response $h_A(z) = |\gamma(2z)|$. For sources having a Gaussian coherence function and using a Gaussian filter function $h_z(\Delta z) = \exp[-4 \ln 2(\Delta z^2/L_z^2)]$, in Eq. (16) we obtain

$$\rho_{P_{MN,\lambda}}(\Delta z) = [h_A(\Delta z) \otimes h_A(\Delta z)] \otimes [h_z(\Delta z) \otimes h_z(\Delta z)] = \exp\left[-4 \ln 2 \frac{\Delta z^2}{2l_c^2 + 2L_z^2}\right] \approx \exp\left(-4 \ln 2 \frac{\Delta z^2}{2L_z^2}\right), \tag{21}$$

where the approximation is valid for $L_z \gg l_c$. Inserting the expression for the speckle contrast into Eq. (20) together with a series expansion in Δz of the approximated ρ from Eq. (21) leads to the following expression for the variance of the attenuation-coefficient estimator:

$$\sigma^2_{\hat{\mu}t} = 4 \ln 2 \left(\frac{4}{\pi} - 1\right) \frac{l_c l_t}{L_z^3 L_t} \equiv K_t \frac{l_c l_t}{L_z^3 L_t}, \tag{22}$$

where all parameters in the last term are geometrical lengths in the sample. As expected, the expression shows that there is a trade-off of transversal and axial resolution against precision in the determined optical properties. More interessting is the important result that according to Eq. (22), the reduction in speckle noise is more efficient when averaging axially than transversally. The origin of this asymmetry is the differentiation in the axial direction, which amplifies high-frequency spatial noise, thus yielding a more efficient averaging in the axial direction than in the transversal direction when using the same filter length.

Using two probing wavelengths, the attenuation coefficients estimated using Eq. (16) can now be used in Eq. (4) to obtain an unbiased estimator for the dye concentration, $\hat{C}_{\mathrm{dye}}(x,z;L_z,L_t)$, in a scattering sample containing an absorbing dye:

$$\hat{C}_{\mathrm{dye}}(x,z;L_z,L_t) = \frac{\hat{\mu}_{t,\lambda_1}(x,z;L_z,L_t) - F\hat{\mu}_{t,\lambda_2}(x,z;L_z,L_t)}{\epsilon_{a,\lambda_1} - F\epsilon_{a,\lambda_2}}. \tag{23}$$

The variance of the estimated dye concentration $\sigma^2_{\hat{C}}$ is given as a function of the variances of the estimated attenuation coefficients:

$$\sigma^2_{\hat{C}} = \frac{\sigma^2_{\hat{\mu}t,\lambda_1} + F^2\sigma^2_{\hat{\mu}t,\lambda_2}}{(\epsilon_{a,\lambda_1} - F\epsilon_{a,\lambda_2})^2}. \tag{24}$$

3 Materials and Methods

3.1 *Tissue Phantoms*

As a simple tissue phantom we use 1.5% Agar gel in Aqua dest, with the addition of Intralipid (IL) to introduce scattering. We created samples having 2-D scattering properties by molding layered samples where the layers have a spatially varying thickness and different IL concentration. As the analyte, we used aluminum phthalocyanine tetrasulfonate chloride (AlPcS834, Porphyrin Products, Inc.), a PDT-related dye with one dominating absorption peak centered at 675 nm. The refractive index of the gel phantoms is $n = 1.34$.

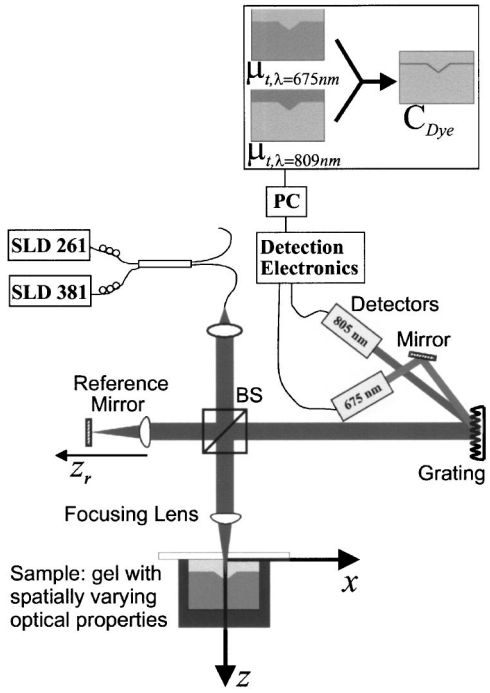

Fig. 1 Wavelength-multiplexed OCT system.

3.2 *Experimental Setup*

Figure 1 shows a simplified schematic of the wavelength-multiplexed OCT system used for acquiring OCT images. The sources are two pigtailed superluminescent diodes (SLDs) from Superlum Diodes. According to data from the manufacturer, they have center wavelengths of 675 and 809 nm, and spectral FWHMs of 10 and 18 nm, respectively. We measured the coherence lengths to be $l_{c,v}=18.1\,\mu$m for the 675-nm source and $l_{c,v}=14.2\,\mu$m for the 809-nm source. These coherence lengths correspond to spectral FWHM of 11 and 20 nm for the 675- and 809-nm sources, respectively, assuming Gaussian spectra. In a sample of group refractive index n_g, the coherence length is reduced to $l_c=l_{c,v}/n_g$. Light from the two sources is multiplexed in a 2×2 integrated fiber coupler and collimated before it is launched into the bulk Michelson interferometer. The interferometer is shot-noise limited and has a dynamic range of 90 dB.

We used focus tracking[31] to ensure that the focus of the probing beam overlaps with the coherence volume of the interferometer. The focusing lens was scanned along with the reference mirror using lens velocity $v_l=v_r/n_g^2$, where v_r is the velocity of the reference mirror. For all the experiments presented, the reference-mirror scanning velocity was $v_r=1$ mm/s.

The light was focused into the sample by a focusing lens (Melles Griot 06GLC003) having focal length $f=14.5$ mm. An identical lens is used in front of the reference mirror in order to match dispersion in the two interferometer arms. Transversal resolution and thus speckle size was determined by the spot size of the focused probing beam, as described in Sec. 2.2. The $1/e^2$ beam diameter was around 5 mm, yielding a theoretical transversal resolution of approximately $l_t\approx2.5\,\mu$m. According to the lens manufacturer, the focusing lens has a focal shift of about 100 μm between the two probing wavelengths, resulting in a degrading of the transversal resolution at one or both wavelengths, depending on the overlap between the focus and the coherence area. Through experiments, we have found that a transversal displacement of 10 μm is sufficient for the speckle signal in two adjacent A scans to be decorrelated at both wavelengths.

Table 1 Optical properties of 1.5% Agar gel and aluminim phthalocyanine dye.

	Definition	Value
F	$\mu_{t,675}/\mu_{t,809}$	1.5 ± 0.05
$\epsilon_{a,675}$	$\mu_{a,675}/C_{\text{dye}}$	44[a] ml/mg mm
$\epsilon_{a,809}$	$\mu_{a,809}/C_{\text{dye}}$	$<10^{-3}\epsilon_{675}$

[a] Typical value. Accurate value determined for each individual stock solution of dye.

4 Experimental Results

Experiments were performed on several sample objects of Agar gel prepared with different concentrations of IL and phthalocyanine dye. Homogenous samples with constant dye and IL concentrations, and one-dimensional (1-D) samples with IL concentration varying only in the z direction were used to investigate the influence of transversal and axial speckle averaging on the precision and resolution in estimating the depth-resolved optical properties. These measurements were also used to study the relation between field reflectivity and scattering coefficient. Two-dimensional cross-sectional images of three-dimensional (3-D) samples with IL concentration varying both in depth and in the plane normal to the optical axis of the probing light were also recorded. Functional images of optical properties and dye concentration were found from the structural OCT images recorded at two wavelengths. Results are presented in the following sections.

4.1 *Determining Tissue-Phantom Parameters*

To determine the dye concentration from the OCT images using Eq. (4), initial measurements were performed to find the necessary parameters for the phantoms. A commercial absorption spectrometer (Agilent 8452 UV-visible spectrophotometer) was used to determine the extinction coefficient of the dye at the two probing wavelengths. Measurements on Agar samples without dye, using the OCT setup, determined an empirical value for F for several IL concentrations. For this purpose, the scattering coefficient was determined, for both wavelengths, by linear regression on the logarithm of the OCT envelope, transversally averaged over a large area of the sample, and Eq. (3) was employed. For all IL concentrations used in the current experiments, the same value for F, within the measurement uncertainty, was found. Experimentally determined values for F and $\epsilon_{a,\lambda}$ are summarized in Table 1. Note that the dye extinction coefficient was found to be more that three orders of magnitude larger at 675 than at 809 nm. In the further calculations, we therefore use $\epsilon_{a,809}=0$.

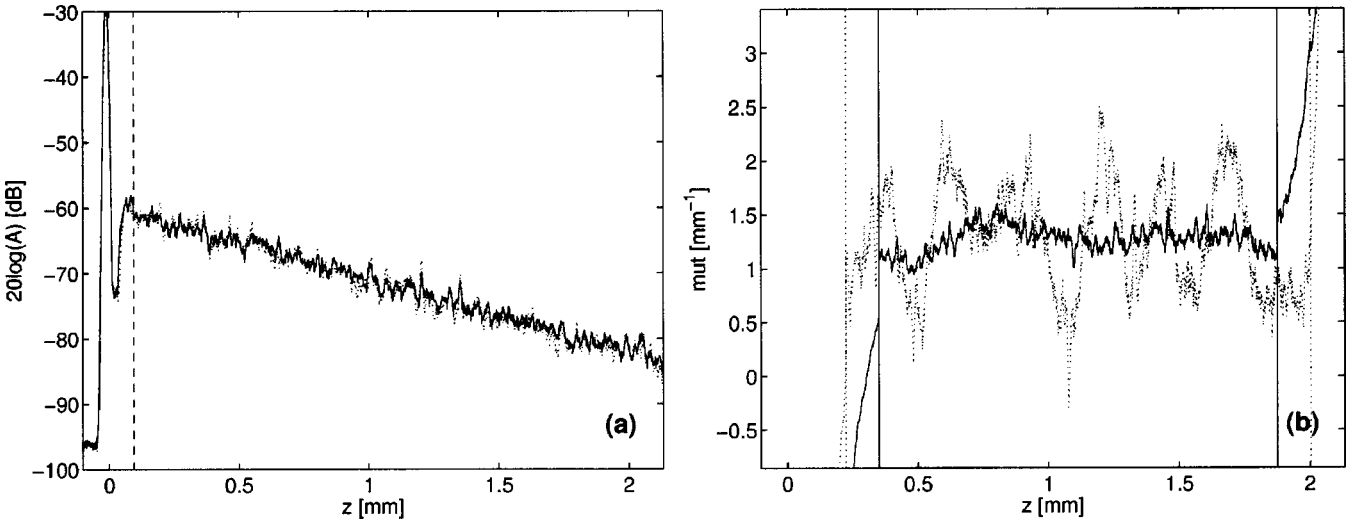

Fig. 2 (a) Logarithm of the transversally speckle-averaged OCT image function $P_{m,675}$ for a sample of Agar gel containing 0.15% IL and (b) estimated depth-resolved attenuation coefficient $\hat{\mu}_t(z;L_z)$ calculated from (a) using Eq. (16). Solid lines represent $m=60$ and $L_z=0.30$ mm, while dotted lines represent $m=30$ and $L_z=0.15$ mm. Data between the two vertical lines are not influenced by edge effects.

4.2 *Speckle Noise in Estimation of the Attenuation Coefficient and Dye Concentration*

To get a qualitative impression of the effect of transversal and axial speckle averaging on the estimated attenuation coefficient, we analyzed OCT images recorded from a homogenous Agar sample containing 0.15% IL. Figure 2(a) shows the logarithm of the image function recorded at 675 nm. The Agar samples were covered with a microscope glass slide, and the dip in the signal right below the glass-Agar reflection is due to a thin layer of water between the glass and the gel. To obtain an estimate of the depth-resolved attenuation coefficient we used Eq. (16). The image function was filtered in the axial direction by convolution with a filter function while no further filtering was done transversally. The axial filter function was chosen to be a Gaussian function truncated at $\pm 2\sigma$. The Gaussian is a common filter function due to its lack of sidelobes in both position and spatial frequency. Truncating it introduces some sidelobes in the spatial-frequency plane, but provides strict control over which parts of the filtered data are affected by edge effects. As characteristic length of the filter function L_z we used the full width at half maximum. Figure 2(b) shows the resulting depth-resolved attenuation coefficient for $m=60$ and $L_z=0.30$ mm (solid line) and $m=30$ and $L_z=0.15$ mm (dotted line) obtained from the data to the right of the vertical dashed line in Fig. 2(a). As expected from Eq. (22) we see that increasing m, and L_z greatly improves the precision in the estimated attenuation coefficient. Note that as long as the backscattered signal is well above the noise level of the system, speckle noise will be the dominating source of noise in the image function. The noise sources defining the noise level of the system will thus not influence the analysis of the variance in the estimated attenuation coefficient.

To quantify the effect of transversal and axial speckle averaging on the precision in the estimated attenuation coefficient $\hat{\mu}_t$, the standard deviation of the estimated depth-resolved attenuation coefficient $\sigma_{\hat{\mu}t}$ was found experimentally for several values of m and L_z. As the axial filter function we used a Gaussian function. The solid lines in Fig. 3 are a contour plot of $\sigma_{\hat{\mu}t}$ determined experimentally from measurements on an Agar sample containing 0.15% IL using the source at 675 nm. The two crosses indicate the parameters used in Fig. 2(b). To compare the experimental results with the theoretical predictions, we plotted the theoretical expression from Eq. (22) along with the experimental results. To obtain the good agreement shown in Fig. 3, the constant K_t in Eq. (22) was multiplied by a factor 1.6. Thus, the deviation between the theoretical predicted and experimentally determined values for the variance in the estimated attenuation

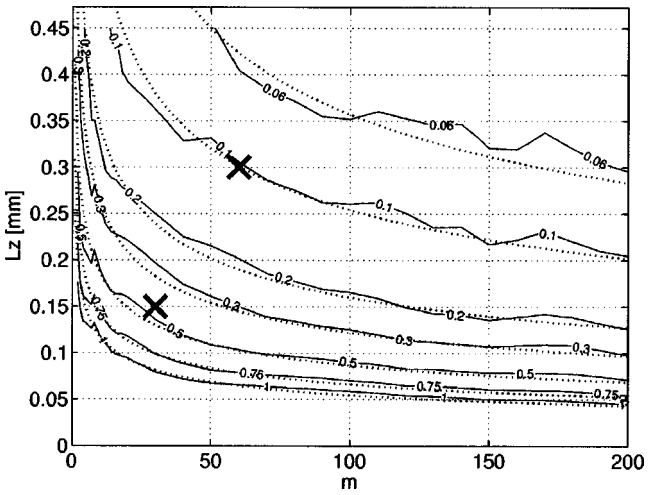

Fig. 3 Contour plot of the experimentally determined standard deviation $\sigma_{\hat{\mu}t}$ mm^{-1} of the estimated, depth-resolved, attenuation coefficient as a function of the number of averaged independent A scans, m, and the FWHM of the axial filter function L_z. Measurements were performed on an Agar sample having $C_{IL}=0.15\%$ IL, corresponding to $\mu_t \approx 1$ mm^{-1}. The two crosses indicate the speckle-averaging parameters used in Fig. 2(b). The dotted lines are contours found using the theoretical expression in Eq. (22) with the constant K_t multiplied by a factor 1.6.

coefficient was 26%. For the 809-nm source, the deviation was found to be 14%.

Next we estimated the depth-resolved attenuation coefficient at both probing wavelengths, and an estimate for the sample dye concentration was found using Eq. (23). Measurements were performed on homogenous Agar samples containing both IL and dye. We prepared samples having three different nominal dye concentrations, $C_{\mathrm{dye}}=0.000$ mg/ml, 0.030 mg/ml, and 0.045 mg/ml, all having the same concentration of IL, $C_{\mathrm{IL}}=0.15\%$. Figure 4(a) shows the average of the OCT envelope of $m=200$ transversally displaced and uncorrelated A scans recorded at 675 and 809 nm for Agar gel having $C_{\mathrm{dye}}=0.030$ mg/ml. The plots clearly show the difference in attenuation at the two wavelengths resulting in a steeper slope for the envelope recorded at 675 nm (black line) than at 809 nm (gray line).

The depth-resolved attenuation coefficient of the samples was determined using Eq. (16) for both wavelengths. Results for the 0.030-mg/ml sample are shown in Fig. 4(b). Again we used a truncated Gaussian function having an FWHM of $L_z=0.25$ mm as an axial filter function. The solid, vertical lines delimit the interval unaffected by edge effects in the filtering. Only the data to the right of the vertical dashed line in Fig. 4(a) were used for estimating the attenuation coefficients.

Using Eq. (23), an estimate of the depth-resolved dye concentration was obtained based on the two depth-resolved attenuation coefficient estimates. Estimated concentrations are plotted in Fig. 4(c) for typical measurements on Agar samples prepared using all three dye concentrations. The dotted horizontal lines show the nominal dye concentration determined from the amount of dye added to the samples during preparation. We see that in the interval where results are unaffected by edge effects, there is good agreement between the nominal and estimated dye concentration, with root mean square (rms) deviations within the interval 0.0033 to 0.0040 mg/ml for the three samples. As expected from Sec. 2.3, the standard deviation of the estimated dye concentration is independent of the value of the dye concentration with an average standard deviation for the three samples being $\langle\sigma_{\hat{C}}\rangle=0.0028$ mg/ml, within the interval unaffected by edge effects. This is in good agreement with the theoretical value $\sigma_{\hat{C}}=0.0022$ mg/ml found from Eq. (24) using the current speckle-averaging and source parameters. The deviation between the experimental and theoretical value probably originates from the deviation found in the analysis of Fig. 3.

4.3 *Spatial Resolution in Determining the Optical Properties*

To study the effect of sample inhomogeneities on the estimation of optical properties, we prepared two-layered Agar samples having different IL concentrations but the same dye concentration in the two layers. Figure 5(a) shows the transversally averaged OCT envelope from a sample having a 1-mm layer where $C_{\mathrm{IL}_1}=0.05\%$ on top of a layer where $C_{\mathrm{IL}_2}=0.15\%$. The dye concentration in both layers is $C_{\mathrm{dye}}=0.030$ mg/ml. Note that there is a step in the level of the backscattered signal at the interface between the two layers due to the increased backscattering, and that the slope of the averaged envelope is steeper in the second than in the first layer. When differentiating a signal such as this, the difference

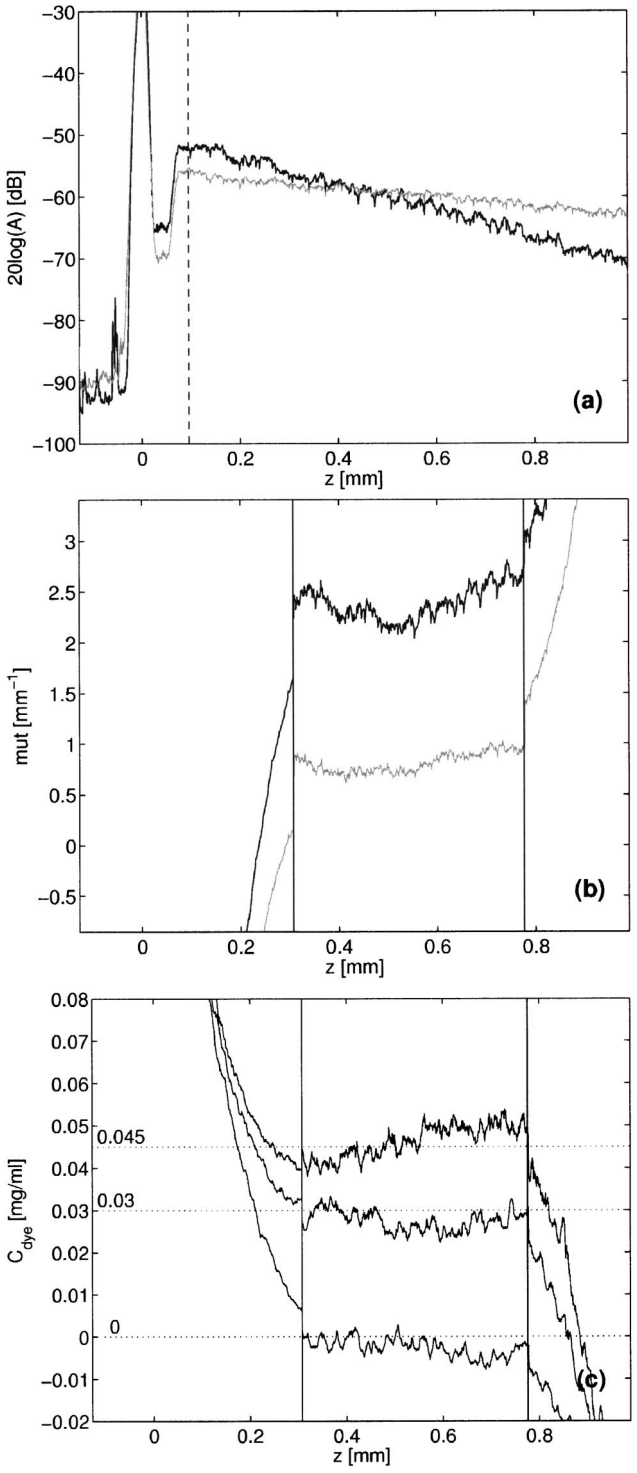

Fig. 4 Experimental results from three homogeneous Agar samples, all with 0.15% IL but different dye concentrations: (a) logarithm of the image function $P_{m,\lambda}$ from a sample having a nominal dye concentration $C_{\mathrm{dye}}=0.030$ mg/ml, the black and gray lines represent data recorded at 675 and 809 nm, respectively, using $m=200$; (b) depth-resolved attenuation coefficient $\hat{\mu}_t(z,L_z)$ estimated from the data in (a) using $L_z=0.25$ mm; and (c) estimated depth-resolved dye concentration $\hat{C}_{\mathrm{dye}}(z)$ calculated from the data in (b) using Eq. (4). In addition to the results from (b), the panel shows results from samples with nominal dye concentrations $C_{\mathrm{dye}}=0.045$ mg/ml and $C_{\mathrm{dye}}=0$ mg/ml. The solid vertical lines in (b) and (c) indicate the area where estimated parameters are unaffected by edge effects.

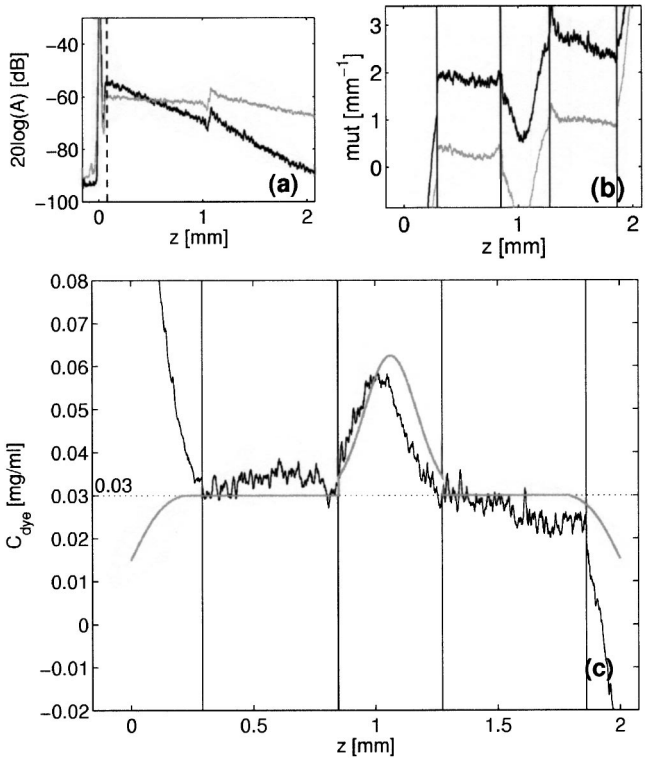

Fig. 5 Results from a two-layered Agar sample having $C_{\mathrm{IL}_1}=0.05\%$ (top layer) and $C_{\mathrm{IL}_2}=0.15\%$ (bottom layer). The interface between the two layers is at $z=1$ mm. Both layers have nominal dye concentration $C_{\mathrm{dye}}=0.030$ mg/ml: (a) logarithm of the image function $P_{m,\lambda}$ for $m=250$ recorded at 675 nm (black line) and 809 nm (gray line); (b) estimated depth-resolved attenuation coefficient $\hat{\mu}_t(z,m,L_z)$, estimated from the data in (a) using $L_z=0.25$ mm; and (c) estimated depth-resolved dye concentration $\hat{C}_{\mathrm{dye}}(z)$, calculated from the data in (b) using Eq. (23). The solid gray line shows a model of the estimated dye concentration.

in signal slope in the two layers will appear as a step function in the differentiated signal, while the step in signal level gives rise to a delta function at the interface. Using Eq. (16), we obtained an estimate of the depth-resolved attenuation coefficient, as plotted in Fig. 5(b). We see the step in attenuation coefficient as we pass from the first to the second layer, and an artifact created by the convolution of the filter function with the delta function in the differentiated envelope. The width of the artifact is equal to the width of the filter function and thus illustrates the spatial resolution in the estimate of the attenuation coefficient. Using Eq. (23), we find an estimate for the depth-resolved dye concentration in the layered sample. The result is plotted in Fig. 5(c). There is good agreement between the nominal and estimated dye concentrations for depths where the results are unaffected by edge effects and the artifact created by the step in backscattered reflectivity. Combining Eqs. (2), (3), (10), (14), and (16) we find a model for the effect of a step in backscattering reflectivity on the estimated dye concentration. The modeled dye-concentration profile for the measurement in Fig. 5 is plotted using a solid gray line in 5(c) and we see that the model gives a good descriptin of the effect of a step in backscattering reflectivity on the estimated dye concentration. For simple objects like this, the step artifact can be eliminated by adjusting the signal level at each side of the boundary to remove the step in signal level. For more complicated samples, this will not be possible and artifacts like this represent a limitation on the spatial resolution of the method.

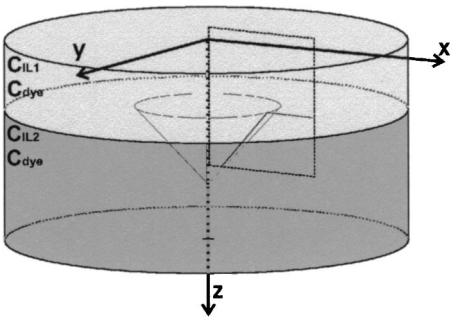

Fig. 6 Schematic illustration of the layered Agar sample. Different concentrations of IL in the C_{IL_1} and C_{IL_2} layers result in a sample with 3-D varying scattering properties. The dye concentration C_{dye} is the same in both layers. The 2-D image area for the structural and functional OCT images is indicated.

4.4 *Functional OCT Images of Dye Concentration*

The preceding results were obtained from measurements on 1-D samples where the optical properties vary only in the axial direction. Prior to estimating the attenuation coefficients and dye concentration, a large number of transversally displaced A scans were averaged, thus severely degrading transversal resolution. To test the ability of the method for imaging dye concentration in more challenging samples, we prepared layered Agar samples with a 3-D variation in scattering properties, as illustrated schematically in Fig. 6. Variation in scattering properties was obtained by using different IL concentrations in the two layers where C_{IL_1} and C_{IL_2} is the IL concentration of the top and bottom layers, respectively. The samples were prepared with the same dye concentration C_{dye} in both layers.

These samples are simple compared to the challenging task of concentration monitoring in tissue. Since the variation in scattering is obtained merely by varying the IL concentration in the two layers, we know that the whole sample has the same F. This assumption might not be generally true for tissue. Tissue will also have a more complicated structure with different-size areas having varying scattering properties. This will complicate the analysis compared to the samples used in the experiment where the scattering properties are homogeneous within each of the two layers.

Figure 7 shows 2-D cross-sectional structural OCT images of a sample prepared using $C_{\mathrm{IL}_1}=0.05\%$, $C_{\mathrm{IL}_2}=0.15\%$, and $C_{\mathrm{dye}}=0.030$ mg/ml recorded at 675 and 809 nm. The image area is indicated by dotted lines in Fig. 6. Attenuation of the signal with depth is more pronounced at 675 than at 809 nm due to the absorption peak of the dye at 675 nm. It is also evident from the structural OCT images that signal attenuation is stronger in the bottom layer than in the top layer, indicating that the scattering coefficient in the bottom layer is larger than in the top layer.

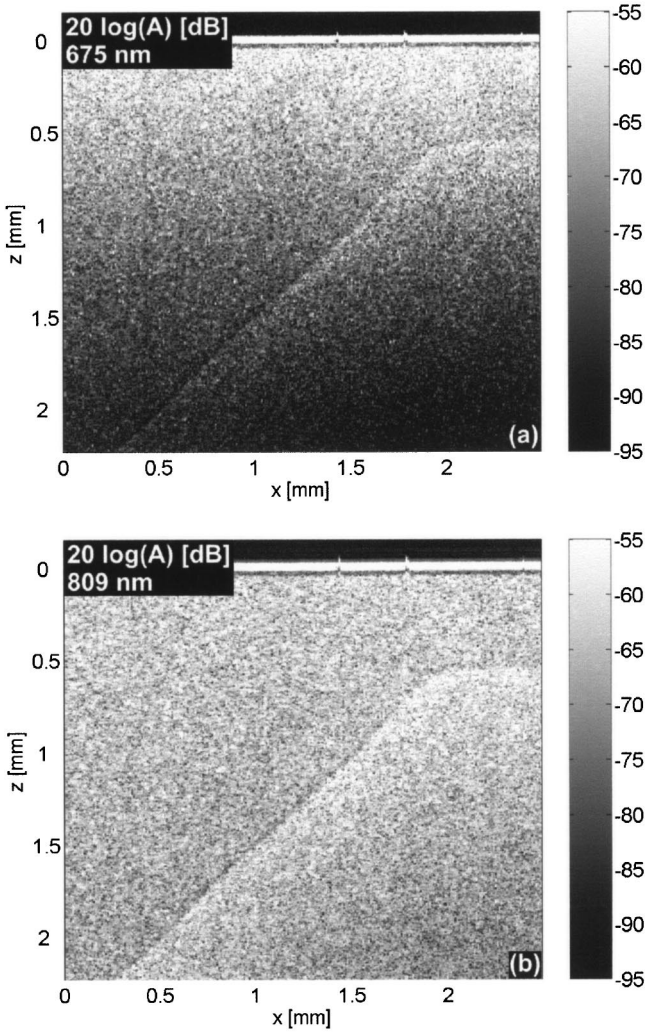

Fig. 7 OCT images of the layered Agar sample of Fig. 6 recorded at two different wavelengths: (a) 675 and (b) 809 nm.

Using Eq. (16) we obtain estimated images of the scattering coefficient at the two wavelengths. Results are shown in Figs. 8(a) and 8(b) for 675 and 809 nm, respectively. The estimated optical properties are obtained using $m=1$ in the image function. The transversal displacement for each A scan is $\Delta x=10\,\mu$m, found experimentally to be large enough to ensure uncorrelated speckle noise in adjacent A scans for both wavelengths. The transversal and axial filter functions are chosen to be Gaussian functions truncated at $\pm 2\sigma$ and normalized to unit area. The characteristic lengths of the filter functions, the FWHM of the Gaussian functions, for the images in Fig. 8 are $L_z=L_t=0.20$ mm. According to Eq. (17), each pixel in the images is thus an average over approximately $N\times M=270$ and 340 independent speckle realizations for the images recorded at 675 and 809 nm, respectively. The interface between the two agar layers can be clearly seen in the images due to the step artifact discussed in Sec. 4.3. The difference in the attenuation coefficient in the two layers is evident in the images, and we can also see that the estimated attenuation coefficient has a constant mean value within each layer.

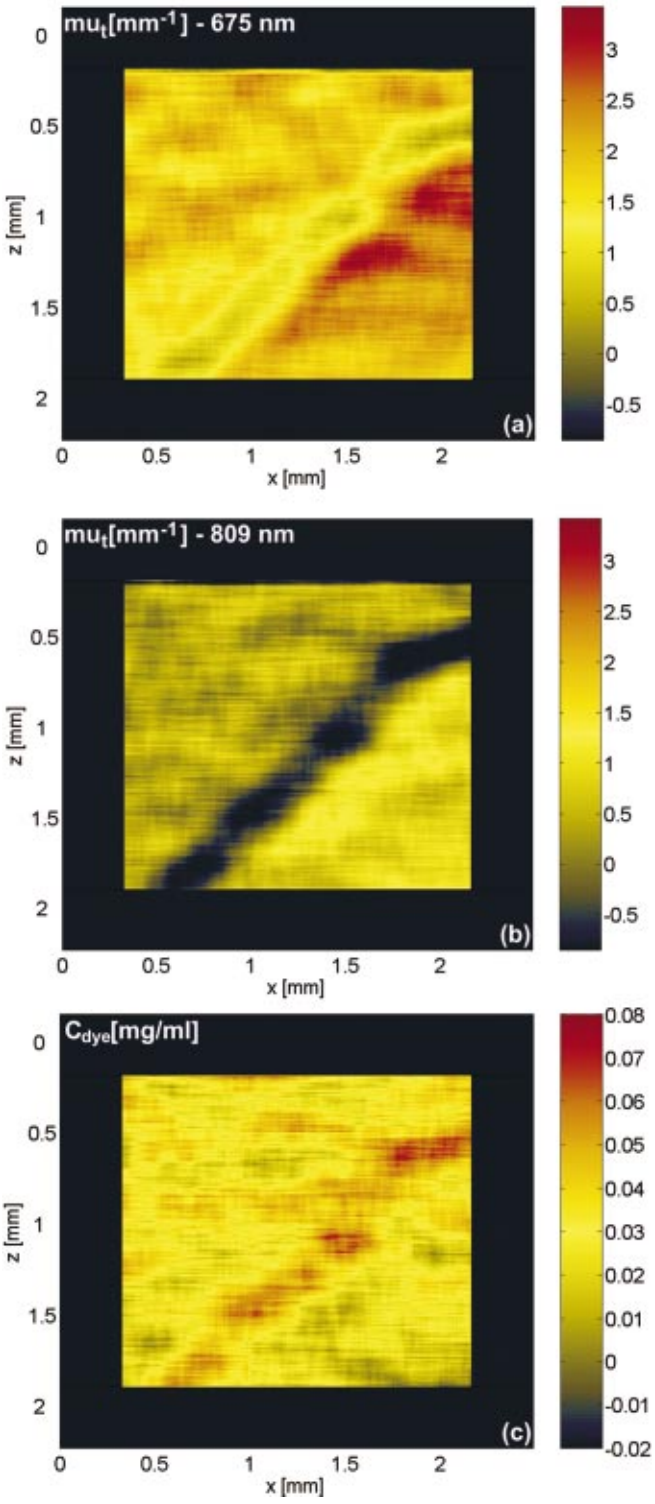

Fig. 8 Functional images of the layered Agar sample in Fig. 6: estimated attenuation coefficient at (a) 675 nm, $\hat{\mu}_{t,675}(x,z;L_z,L_t)$ and (b) 809 nm, $\hat{\mu}_{t,809}(x,z;L_z,L_t)$; (c) estimated dye concentration $\hat{C}_{\text{dye}}(x,z;L_z,L_t)$. The FWHM of the transversal and axial filter functions are $L_z=L_t=0.20$ mm. The dark-blue border around the images masks the parts of the images influenced by edge effects.

Finally, Fig. 8(c) shows functional OCT images of estimated dye concentration calculated from Figs. 8(a) and 8(b) using Eq. (23). Apart from the artifact arising from the interface between the two layers, the image shows a fairly constant

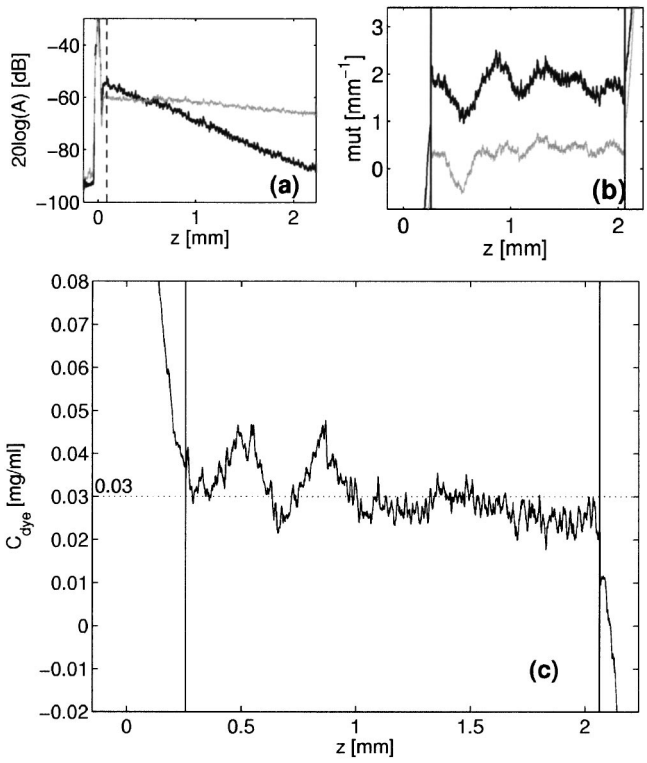

Fig. 9 (a) Logarithm of the image function $P_{m,\lambda}$, $m=250$, obtained by averaging all A scans of Figs. 7(a) (black line) and 7(b) (gray line); (b) estimated attenuation coefficient at the two wavelengths based on the image functions in (a), $L_z=0.20$ mm; and (c) estimated dye concentration calculated from the estimated attenuation coefficients in (b). We observe that even though the scattering of the sample varies transversally along the sample, the resulting calculated depth-resolved dye concentration is in good agreement with the theoretical value as a function of depth.

dye concentration. The estimated dye concentration averaged over the two sample layers, excluding edge and interface regions, is $\langle \hat{C}_{\mathrm{dye}} \rangle = 0.028$ mg/ml with a standard deviation of $\sigma_C = 0.010$ mg/ml, compared to nominal value $C_{\mathrm{dye}} = 0.030$ mg/ml.

The functional dye-concentration image shows that even though the experimental results are in good agreement with the expected value within the two layers, the step in reflectivity at the layer interface influences a significant part of the image. For more realistic tissue phantoms and, eventually, for measurements on tissue, it might be expected that local variation in reflectivity may corrupt the dye-concentration images. Figure 9(a) shows the transversally averaged OCT envelope for the data presented in Figs. 7 and 8. In Figs. 9(b) and 9(c) the attenuation coefficient and the dye concentration are calculated following the same procedure as used in Sec. 4.2. Figure 9(c) shows that even though the scattering of the sample varies transversally, the resulting calculated depth-resolved dye concentration is in good agreement with the nominal value. The mean value of the estimated dye concentration is $\langle C_{\mathrm{dye}} \rangle = 0.030$ mg/ml and the standard deviation is $\sigma_{\hat{C}} = 0.005$ mg/ml. This is an indication that even for samples having large variations in scattering properties, it may be possible to obtain reliable estimates of the dye concentration at the expense of transversal resolution, if only the scattering properties vary within the limitation of the model as it is presented in Sec. 2.1.

5 Discussion

The presented results show that it is possible to obtain functional images of the concentration of an analyte in a scattering Agar-IL tissue phantom based on OCT measurements at two wavelengths. The following is a discussion of factors determining the precision in the estimated dye concentration and some of the challenges in the design of a dual-wavelength concentration-imaging OCT system.

In this paper, speckle averaging is limited to spatial averaging, and we do not discuss speckle-noise reduction through polarization diversity,[32] frequency compounding,[23] or advanced image processing.[33] As a measure of precision in the estimated attenuation coefficients and dye concentration, we use the variance of the estimated parameters. According to Eq. (22), the variance of $\hat{\mu}_t$ is proportional to the source coherence length l_c and the transversal resolution l_t, inversely proportional to the width of the transversal filter function L_t, and inversely proportional to the third power of the width of the axial filter function L_z. Thus, there is a trade-off between spatial resolution and precision in the estimated attenuation coefficient. An increase of the axial filter width gives a larger improvement in precision compared to the same increase in transversal filter width. Imaging with a shorter coherence length, or a larger numerical aperture, will reduce speckle size in the axial and transversal directions, respectively. For a given spatial resolution, determined by the filter lengths, the precision in the estimated attenuation coefficient will thus be improved because the number of independent speckles within the filter lengths increases. A shorter coherence length can be obtained using a broader bandwidth source as long as dispersion in the sample under study is small enough to avoid problems due to dispersion broadening.

Few studies have been done on the precision of estimated attenuation coefficients from tissue. Schmitt et al.[12] report values of the attenuation coefficient of human tissue from different sites on the body determined with an average standard deviation of $\sigma_\mu \approx 0.5\ \mathrm{mm}^{-1}$. The attenuation coefficient at the different sites varied in the range 2 to 5 mm^{-1}. This result was obtained using linear regression over $L_d = 0.50$ mm with no transversal averaging of the OCT envelope, and is of the same order of magnitude as σ_μ predicted by the expression in Eq. (22). Kholodnykh et al.[34] state that they have determined the scattering coefficient of tissue with a precision of 0.8%, corresponding to a standard deviation of $\sim 0.05\ \mathrm{mm}^{-1}$ for typical values of the scattering coefficient of tissue. To achieve this precision 5×10^4 A scans were averaged over a transversal area of 3.4×4.3 mm, and the attenuation coefficient was found as the slope of the logarithm of the averaged data using linear regression over a depth of 0.25 mm. For these averaging parameters, and a reported coherence length of $l_c = 15\ \mu$m, Eq. (22) predicts a theoretical standard deviation of $\sim 0.004\ \mathrm{mm}^{-1}$, thus is an order of magnitude better than estimated by Kholodnykh et al.

Typical values for the attenuation coefficient of human tissues are $>1\ \mathrm{mm}^{-1}$. Equation (22) shows that for a coherence length in the sample of 15 μm and a transversal resolution of 10 μm, a variance in the estimated attenuation coefficient of

$\sigma_{\hat{\mu}} = 0.01\ \mathrm{mm}^{-1}$ is obtained for $L_z = L_t = 1.03$ mm. Reducing the filter lengths to $L_z = L_t = 0.46$ mm results in a variance of $\sigma_{\hat{\mu}} = 0.05\ \mathrm{mm}^{-1}$. These results are obtained on samples having an attenuation coefficient of 1 to 2.5 mm^{-1}, just within realistic values for human tissues. For samples having a higher attenuation coefficient, the object depth for which we have a useful signal will be reduced. This limits the maximum filter length and thereby the precision in the attenuation-coefficient estimator.

Equations (22) and (24) show that the precision in the estimated dye concentration is independent of the dye concentration value. This is confirmed by experimental results presented in Fig. 4(c). For a given set of speckle-averaging parameters, the resulting precision represents a fundamental limit on detectability of low dye concentrations. Equation (24) expresses how the variance in $\hat{C}_{\mathrm{dye}}$ depends on the variance in $\hat{\mu}_t$. The choice of probing wavelengths and thus the values of F, ϵ_{a,λ_1}, and ϵ_{a,λ_2} together with $\sigma^2_{\hat{\mu},\lambda_i}$ determine the precision of the estimated dye concentration. According to Eq. (22) the variance in $\hat{\mu}_t$ is determined by the speckle-averaging parameters, transversal resolution, and the source coherence length. Assuming that we can choose source parameters giving $\sigma^2_{\hat{\mu}t\lambda_1} \cong \sigma^2_{\hat{\mu}t\lambda_2} = \sigma^2_{\hat{\mu}}$, for any F, and introducing the parameter $E = \epsilon_{a,\lambda_2}/\epsilon_{a,\lambda_1}$, Eq. (24) simplifies to $\sigma^2_{\hat{C}} = K_\sigma(1+F^2)/(1-EF)^2$, where $K_\sigma = \sigma^2_\mu/\epsilon^2_{a,\lambda_1}$. When imaging a dye having a narrow absorption band centered at λ_1 and $E = 0$, the second probing wavelength λ_2 should be chosen to yield $F < 1$, i.e., the scattering at λ_2 should be larger than at λ_1. This will give an improved precision in $\sigma_{\hat{C}}$ compared to using a wavelength yielding $F > 1$. For the sources used in this paper, $F > 1$. Generally the best precision in $\hat{C}_{\mathrm{dye}}$ is obtained when both F and E are $\ll 1$. An additional requirement is that the total attenuation at both wavelengths must be weak enough to give a sufficiently large penetration depth for good determination of the slope of the OCT envelope.

The presented method is limited to samples with relatively homogeneous scattering. The whole sample is represented by the same F, and this F value is assumed not to change with concentration of the analyte under study. Faber et al. showed that blood oxygenation changes the scattering properties of whole blood.[35] An effect of this kind will complicate the analysis. In addition, the dye must be the only absorbing component in the sample. This will not generally be the case for tissue where several other chromophores (e.g., hemoglobin and melanin) may contribute to the absorption, thus complicating the selection of suitable wavelengths.

A challenge when using two or more probing wavelengths in the interferometer lies in the choice of optical components. Unless the focusing lens is completely corrected for chromatic abberations at all probing wavelengths, differences in focal length will result in degraded transversal resolution at all but one of the wavelengths, since the coherence area can not overlap with the focus area for all wavelengths simultaneously. Dispersive samples will complicate the situation further since the coherence area will be located at different geometrical depths for different wavelengths.

Note that Eq. (16) includes an additional implicit approximation in assuming that all the light recorded at depth z has traveled the same path length in the sample. This approximation will be increasingly inaccurate as the numerical aperture (NA) for the system increases and light passing through the outer part of the aperture may have traveled a significantly longer distance in the object than light traveling close to the optic axis. For large-NA systems, this will give an incorrect estimate of the attenuation coefficient if not corrected for.

Focus tracking is necessary to extract quantitative information about the attenuation coefficient of a sample from OCT images. An alternative to focus tracking is correcting the recorded data for the effect of the confocal function.[14,34] For samples with relatively high scattering, focus tracking is the better alternative since it gives a larger penetration depth, enabling more axial filtering and thus better precision in the determined optical properties. Finally, a large dynamic measurement range is required for high penetration depth.

This work was carried out using a dual-source interferometer with wavelengths tuned to the analyte under study. An OCT system using an ultrabroadband source would enable measurements at a wide range of wavelength bands, providing a flexible solution for imaging of analytes with different absorption properties.

6 Conclusion

This paper demonstrated quantitative functional imaging of the concentration of an absorbing analyte in a scattering tissue phantom by means of spectroscopic OCT. We analyzed the accuracy of the dye-concentration estimate and discussed sources of error that apply to the measurements. Good agreement was demonstrated between measured and predicted variances in the estimated attenuation coefficients and dye concentration. We presented guidelines for spectroscopic OCT systems for concentration imaging and discussed some of the possible obstacles for the application of the method to more realistic phantoms and tissue. Tissue is a complicated sample and it is difficult to predict what will be the dominating obstacles when using this method on live tissue. Nevertheless, this paper demonstrated that the goal of quantitative depth-resolved measurements of dye concentration is, in principle, possible to achieve provided that a sufficient model for the optical properties of the tissue is found.

Acknowledgments

This work was supported by the Research Council of Norway. The authors wish to thank Prof. Ole J. Løkberg and Prof. Hans M. Pedersen for helpful discussions on instrumentation and speckle averaging, respectively.

References

1. W. Drexler, U. Morgner, F. Kärtner, C. Pitris, S. Boppart, X. Li, E. Ippen, and J. Fujimoto, "In vivo ultrahigh-resolution optical coherence tomography," *Opt. Lett.* **24**, 1221–1223 (1999).
2. W. Drexler, "Ultrahigh-resolution optical coherence tomography," *J. Biomed. Opt.* **9**, 47–74 (2004).
3. A. Dubois, L. Vabre, A. C. Boccara, and E. Beaurepaire, "High-resolution full-field optical coherence tomography with a linnik microscope," *Appl. Opt.* **41**, 805–812 (2002).
4. Z. Chen, T. Milner, S. Srinivas, X. Wang, A. Malekafzali, M. van Gemert, and J. Nelson, "Non-invasive imaging of *in vivo* blood flow velocity using optical doppler tomography," *Opt. Lett.* **22**, 1–3 (1997).
5. J. F. deBoer, T. Milner, M. vanGemert, and J. Nelson, "Two dimensional birefringence imaging in biological tissue by polarisation sensitive optical coherence tomography," *Opt. Lett.* **22**, 934–936 (1997).

6. R. Weissleder and U. Mahmood, ''Molecular imaging,'' *Radiology* **219**, 316–333 (2001).
7. D. A. Benaron, ''The future of cancer imaging,'' *Cancer Metastasis Rev.* **21**, 45–78 (2002).
8. M. Kulkarni and J. Izatt, ''Spectroscopic optical coherence tomography,'' *OSA Tech. Digest Ser.* **9**, 59–60 (1996).
9. J. Schmitt, S. Xiang, and K. Yung, ''Differential absorption imaging with optical coherence tomography,'' *J. Opt. Soc. Am. A* **15**, 2288–2296 (1998).
10. U. Morgner, W. Drexler, F. Kärtner, X. Li, C. Pitris, E. Ippen, and J. Fujimoto, ''Spectroscopic optical coherence tomography,'' *Opt. Lett.* **25**, 111–113 (2000).
11. D. Faber, E. Mik, M. Alders, and T. von Leeuwen, ''Light absorption of (oxy-)hemoglobin assessed by spectroscopic optical coherence tomography,'' *Opt. Lett.* **28**, 1436–1438 (2003).
12. J. M. Schmitt, A. Knüttel, and R. F. Bonner, ''Measurement of optical properties of biological tissues by low-coherence interferometry,'' *Appl. Opt.* **32**, 6032–6042 (1993).
13. Y. Pan, R. Birngruber, J. Rosperich, and R. Engelhardt, ''Low-coherence optical tomography in turbid tissue: theoretical analysis,'' *Appl. Opt.* **34**, 6564–6574 (1995).
14. J. M. Schmitt and A. Knüttel, ''Model of optical coherence tomography of heterogeneous tissue,'' *J. Opt. Soc. Am. A* **14**, 1231–1242 (1997).
15. S. R. Thurber, A. M. Brodsky, and L. W. Burgess, ''Characterization of random media by low-coherence interferometry,'' *Appl. Spectrosc.* **54**, 1506–1514 (2000).
16. A. I. Kholodnykh, I. Y. Petrova, K. V. Larin, M. Motamedi, and R. O. Esenaliev, ''Precision of measurement of tissue optical properties with optical coherence tomography,'' *Appl. Opt.* **42**, 3027–3037 (2003).
17. T. Støren, D. Östling, L. O. Svaasand, O. J. Løkberg, and T. Lindmo, ''Absorption measurements using low coherence interferometry,'' *Proc. SPIE* **3567**, 130–138 (1998).
18. U. Sathyam, B. Colston, L. DaSilva, and M. Everett, ''Evaluation of optical coherence quantitation of analytes in turbid media by use of two wavelengths,'' *Appl. Opt.* **38**, 2097–2104 (1999).
19. M. Pircher, E. Götzinger, R. Leitgeb, A. F. Fercher, and C. K. Hitzenberger, ''Measurement and imaging of water concentration in human cornea with differential absorption optical coherence tomography,'' *Opt. Express* **11**, 2190–2197 (2003).
20. T. Støren, A. Simonsen, O. Løkberg, T. Lindmo, L. Svaasand, and A. Røyset, ''Measurement of dye diffusion in agar gel by use of low-coherence interferometry,'' *Opt. Lett.* **28**, 1215–1217 (2003).
21. J. M. Schmitt, S. H. Xiang, and K. M. Yung, ''Speckle in optical coherence tomography,'' *J. Biomed. Opt.* **4**, 95–105 (1999).
22. A. F. Fercher, W. Drexler, C. K. Hitzenberger, and T. Lasser, ''Optical coherence tomography—principles and applications,'' *Rep. Prog. Phys.* **66**, 239–303 (2003).
23. M. Pircher, E. Götzinger, R. Leitgeb, A. F. Fercher, and C. K. Hitzenberger, ''Speckle reduction in optical coherence tomography by frequency compounding,'' *J. Biomed. Opt.* **8**, 565–569 (2003).
24. D. J. Smithies, T. Lindmo, Z. P. Chen, J. S. Nelson, and T. E. Milner, ''Signal attenuation and localization in optical coherence tomography studied by Monte Carlo simulations,'' *Phys. Med. Biol.* **43**, 3025–3044 (1998).
25. C. K. Hitzenberger, W. Drexler, A. Baumgartner, and A. F. Fercher, ''Dispersion effects in partial coherence interferometry: implications for intraocular ranging,'' *J. Biomed. Opt.* **4**, 144–151 (1999).
26. D. Östling, T. Støren, A. Røyset, O. J. Løkberg, L. O. Svaasand, and T. Lindmo, ''Multiple-depth probing by wavelength multiplexed low coherence interferometry,'' *Proc. SPIE* **4251**, 71–75 (2001).
27. J. W. Goodman, *Laser Speckle and Related Phenomena*, J. C. Dainty, Ed., pp. 9–75, Springer (1984).
28. J. W. Goodman, *Statistical Optics*, Wiley, New York (1985).
29. A. Ishimaru, *Wave Propagatin and Scattering in Random Media*, Vol. 2, Academic Press, New York (1978).
30. H. Stark and F. B. Tuteur, *Modern Electrical Communications, Theory and Systems*, Prentice/Hall International, (1979).
31. Z. Chen, T. Milner, and J. Nelson, ''Optical doppler tomographic imaging of fluid flow velocity in highly scattering media,'' *Opt. Lett.* **22**, 64–66 (1997).
32. J. F. de Boer, S. M. Srinivas, B. H. Park, T. H. Pham, Z. P. Chen, T. E. Milner, and J. S. Nelson, ''Polarization effects in optical coherence tomography of various biological tissues,'' *IEEE J. Sel. Top. Quantum Electron.* **5**, 1200–1204 (1999).
33. J. M. Schmitt, ''Restoration of optical coherence images of living tissue using the clean algorithm,'' *J. Biomed. Opt.* **3**, 66–75 (1998).
34. A. I. Kholodnykh, I. Y. Petrova, K. V. Larin, M. Motamedi, and R. O. Esenaliev, ''Optimization of low coherence interferometry for quantitative analysis of tissue optical properties,'' *Proc. SPIE* **4624**, 36–46 (2002).
35. D. J. Faber, M. C. Aalders, E. G. Mik, B. A. Hooper, and T. G. vanLeeuwen, ''Oxygen saturation dependent optical properties of whole blood,'' *Proc. SPIE* **5316**, 78–84 (2004).